PHYSICAL REVIEW D **88,** 055025 (2013)

Update on scalar singlet dark matter

James M. Cline[*] and Pat Scott[†]
Department of Physics, McGill University, 3600 Rue University, Montréal, Québec H3A 2T8, Canada

Kimmo Kainulainen[‡]
Department of Physics, University of Jyväskylä, P.O.Box 35 (YFL), Jyväskylä FIN-40014, Finland and Helsinki Institute of Physics, University of Helsinki, P.O. Box 64, Helsinki FIN-00014, Finland

Christoph Weniger[§]
GRAPPA Institute, University of Amsterdam, Science Park 904, 1098 GL Amsterdam, Netherlands
(Received 25 June 2013; published 27 September 2013)

One of the simplest models of dark matter is where a scalar singlet field S comprises some or all of the dark matter and interacts with the standard model through an $|H|^2S^2$ coupling to the Higgs boson. We update the present limits on the model from LHC searches for invisible Higgs decays, the thermal relic density of S, and dark matter searches via indirect and direct detection. We point out that the currently allowed parameter space is on the verge of being significantly reduced with the next generation of experiments. We discuss the impact of such constraints on possible applications of scalar singlet dark matter, including a strong electroweak phase transition, and the question of vacuum stability of the Higgs potential at high scales.

DOI: 10.1103/PhysRevD.88.055025 PACS numbers: 95.35.+d, 12.60.Fr, 14.80.Bn

I. INTRODUCTION

Scalar singlet dark matter [1–3] is an attractive model due to its simplicity; the essential couplings are just its bare mass term and a cross-coupling to the standard model (SM) Higgs field,

$$V = \frac{1}{2}\mu_S^2 S^2 + \frac{1}{2}\lambda_{hS} S^2 |H|^2. \tag{1}$$

After electroweak symmetry breaking, the S boson mass receives contributions from both terms, giving

$$m_S = \sqrt{\mu_S^2 + \frac{1}{2}\lambda_{hS} v_0^2}, \tag{2}$$

where $v_0 = 246.2$ GeV is the Higgs vacuum expectation value (VEV). Phenomenology of this model has been studied in Refs. [4–23].

The Higgs cross-term is generically expected to be present because it is a dimension-4 operator that is not forbidden by any symmetry. Apart from the S kinetic term and its quartic self-coupling (which plays no observable role in phenomenology), the two terms in Eq. (1) are in fact the only renormalizable terms allowed by general symmetry arguments. Terms cubic or linear in S are excluded if one demands that S is absolutely stable, and therefore a viable dark matter (DM) candidate, by imposing the Z_2 symmetry $S \to -S$. In this scenario, S is a classic weakly interacting massive particle (WIMP); although it is possible to make S a viable, metastable DM candidate without the Z_2 symmetry, here we focus exclusively on the stable case.

The single $S^2|H|^2$ coupling is, however, enough to allow for a contribution to the invisible decay of the Higgs boson, scattering of S on nucleons through Higgs exchange, and annihilation of S into SM particles, leading to indirect detection signatures and an allowed thermal relic density. The scalar singlet model with Z_2 symmetry is, in essence, the simplest possible UV-complete theory containing a WIMP. It is intriguing that natural values of $\lambda_{hS} \lesssim 1$ and m_S below a few TeV[1] simultaneously reproduce the observed DM relic density and predict a cross section for scattering on nucleons that is not far from the current direct detection limit.

These aspects have of course been widely studied, with Refs. [25–28] providing the most recent comprehensive analyses. We believe it is worthwhile to update the results presented there, for several reasons:

(1) Some [25,26] were done before the mass of the Higgs boson was measured by ATLAS and CMS, and the dependence of the results on m_h was shown for only a limited number of Higgs masses.
(2) With the exception of Ref. [28], these recent studies were performed prior to the release of updated direct detection constraints by the XENON100 Collaboration [29].

[*]jcline@physics.mcgill.ca
[†]patscott@physics.mcgill.ca
[‡]kimmo.kainulainen@jyu.fi
[§]c.weniger@uva.nl

[1]These upper limits based on perturbativity in the λ_{hS} coupling are more stringent than the unitarity bounds on the annihilation cross section [24].

(3) The predicted direct detection cross section depends on the Higgs-nucleon coupling. Recent results from lattice studies [30–40] and chiral perturbation theory [41–47] have reduced the theoretical uncertainty in this quantity.
(4) Limits on the invisible width of the Higgs have improved [48] since all of the recent studies of this model, reducing the allowed parameter space in the region $m_S < m_h/2$.
(5) The constraints on λ_{hS} from direct detection presented by Refs. [25,27,28] and from indirect detection in Ref. [28] were derived without taking into account the fact that larger values of λ_{hS} suppress the S relic density by increasing the annihilation cross section. This reduces the overall predicted signal for scattering on nucleons and annihilation into SM particles. Because of this effect, the dependence on λ_{hS} of the direct and indirect detection constraints is significantly different than one might have expected, as noted in Ref. [26]. We take the view here that singlet dark matter might provide only a fraction of the total dark matter density, which is a logical possibility.
(6) In some previous studies (e.g., Ref. [26]), the relic density has not been computed using the full thermal average of the annihilation cross section. It is necessary to do so when m_S is near $m_h/2$ in order to obtain accurate results because the integral over DM velocities is sensitive to the degree of overlap with the resonance in $\sigma v_{\rm rel}$ at center-of-mass energy $E_{\rm CM} = m_h$. This can change the result by orders of magnitude in comparison to using the threshold approximation.
(7) So far, Ref. [28] has been the only comprehensive study of scalar singlet DM to consider recent indirect detection constraints. The most important of these are gamma-ray constraints from Fermi observations of dwarf galaxies. Reference [28] implemented these limits in an approximate fashion, rescaling published 95% limits on the cross sections for annihilation into an incomplete set of SM final states and ignoring the $SS \to hh$ channel. Here, we calculate constraints self-consistently for the complete set of branching fractions to SM final states at every point of the parameter space, adding further constraints from the impact of SS annihilation on the cosmic microwave background (CMB) and providing projected constraints including the impact of the Čerenkov Telescope Array (CTA).

In the following, we outline updated constraints and projections from the Higgs invisible width (Sec. II), the S thermal relic density (Sec. III), indirect detection (Sec. IV), and direct detection (Sec. V). The relevance of these constraints to some applications of the model is discussed in Sec. VI. We give conclusions in Sec. VII.

II. HIGGS INVISIBLE WIDTH

For $m_S < m_h/2$, the decay $h \to SS$ is kinematically allowed and contributes to the invisible width $\Gamma_{\rm inv}$ of the Higgs boson. The LHC constraints on $\Gamma_{\rm inv}$ continue to improve as the properties of the Higgs boson are shown to be increasingly consistent with SM expectations. Reference [48] obtains a limit of 19% for the invisible branching fraction at 2σ, based on a combined fit to all Higgs production and decay channels probed by ATLAS, CMS, and the Tevatron.

The contribution to $\Gamma_{\rm inv}$ in the scalar singlet dark matter model is

$$\Gamma_{\rm inv} = \frac{\lambda_{hS}^2 v_0^2}{32\pi m_h}(1 - 4m_S^2/m_h^2)^{1/2}, \tag{3}$$

(this corrects a factor of 2 error in Eq. (3.2) of Ref. [49]). To compute the branching fraction $\Gamma_{\rm inv}/(\Gamma_{\rm vis} + \Gamma_{\rm inv})$, we take the visible contribution to the width to be $\Gamma_{\rm vis} = 4.07$ MeV for $m_h = 125$ GeV.

In the left panel of Fig. 1, we show the limit imposed on the scalar singlet parameter space by the invisible width constraint. For $m_S < m_h/2$, couplings larger than $\lambda_{hS} \sim 0.02$–0.03 are ruled out. Here, we also show the region of parameter space that is projected to be in more than 1σ tension with data if no additional Higgs decays are detected at the 14 TeV LHC after 300 fb^{-1} of luminosity has been collected. This corresponds to a limit of 5% on the invisible Higgs branching fraction [50].

III. RELIC DENSITY

The relic density of singlet dark matter is mostly determined by Higgs-mediated s-channel annihilation into SM particles. A subdominant role is played by annihilation into hh, via the direct 4-boson h^2S^2 vertex and S exchange in the t channel. As discussed in Ref. [49], tree-level calculations for SS annihilation into two-body final states do not give a very accurate approximation close to the threshold for producing gauge boson pairs, as they miss the 3- and 4-body final states from virtual boson decays as well as QCD corrections for quarks in the final state. However, this can be overcome by using accurate computations of the full Higgs boson width as a function of invariant mass $\Gamma(m_h^*)$ from Ref. [51] and factorizing the cross section for annihilation into all SM particles except h as

$$\sigma v_{\rm rel} = \frac{2\lambda_{hS}^2 v_0^2}{\sqrt{s}} |D_h(s)|^2 \Gamma_h(\sqrt{s}), \tag{4}$$

where

$$|D_h(s)|^2 \equiv \frac{1}{(s - m_h^2)^2 + m_h^2 \Gamma_h^2(m_h)}. \tag{5}$$

For $m_S < m_h/2$, the width in the propagator $D_h(s)$ (but not elsewhere) must be increased by the invisible contribution due to $h \to SS$. For $m_S > m_h$, Eq. (4) must be supplemented

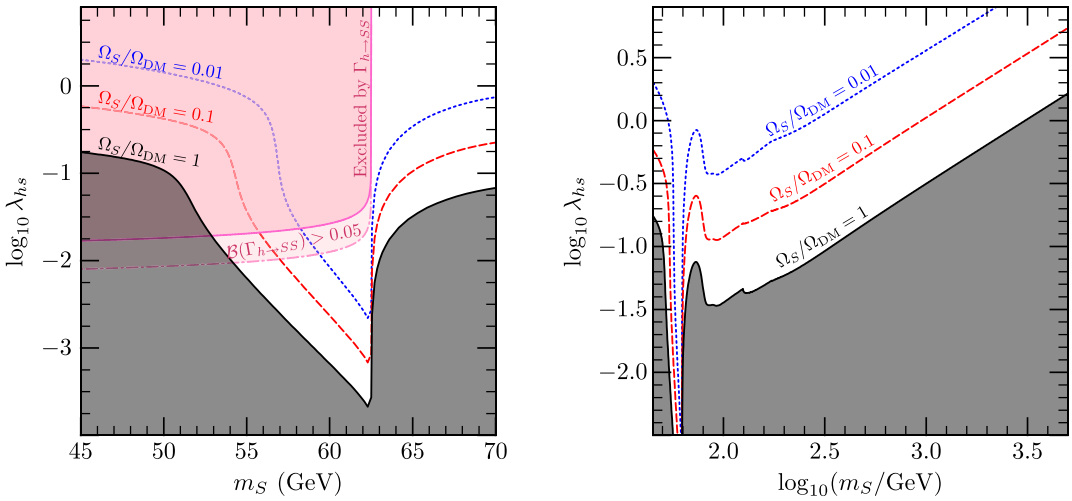

FIG. 1 (color online). Contours of fixed relic density, labelled in terms of their fraction of the full dark matter density. Dark-shaded lower regions are ruled out because they produce more than the observed relic density of dark matter. Left: a closeup of the mass region $m_S \sim m_h/2$, where annihilations are resonantly enhanced. The region ruled out by the Higgs invisible width at 2σ C.L. is indicated by the darker-shaded region in the upper left-hand corner. The projected 1σ constraint from 300 fb^{-1} of luminosity at the 14 TeV LHC is shown as the lighter-shaded region, corresponding to a limit of 5% on the Higgs branching fraction to invisible states [50]. Right: relic density contours for the full range of m_S.

by the extra contribution from $SS \to hh$. The perturbative tree-level result for the $SS \to hh$ cross section is given in Appendix A.

The tabulation of $\Gamma_h(m_h^*)$ in Ref. [51] assumes that m_h^* is the true Higgs mass, associated with a self-coupling $\lambda = (m_h^*)^2/2v_0^2$. Here, $\lambda \approx 0.13$ is fixed by the true Higgs mass, however, and we find that, for $\sqrt{s} \gtrsim 300$ GeV, we must revert to perturbative expressions for $\Gamma_h(\sqrt{s})$, or otherwise the Higgs 1-loop self-interactions included in the table of Ref. [51] begin to overestimate the width. Above $m_S = 150$ GeV, we revert to the tree-level expressions for the decay width, including all SM final states. The expressions we use can again be found in Appendix A.

To accurately determine the relic density for m_S in the vicinity of the resonance at $4m_S^2 \sim m_h$ in Eq. (4), it is essential to carry out the actual thermal average [52]

$$\langle \sigma v_{\text{rel}} \rangle = \int_{4m_S^2}^{\infty} \frac{s\sqrt{s-4m_S^2}K_1(\sqrt{s}/T)\sigma v_{\text{rel}}}{16Tm_S^4K_2^2(m_S/T)}\,\mathrm{d}s, \quad (6)$$

where K_1, K_2 are modified Bessel functions of the second kind, and to solve the Boltzmann equation for the relic abundance [53].

The common approximation of setting the threshold value of σv_{rel} to the standard value of 1 pb $\cdot$ c fails badly close to the resonance. This is because the integral in Eq. (6) can be dominated by the resonance at $s = m_h^2$ even if m_S is considerably below $m_h/2$, possibly increasing $\langle \sigma v_{\text{rel}} \rangle$ by orders of magnitude relative to the threshold value. If $m_S \gtrsim m_h/2$, the thermal averaging pushes $\langle \sigma v_{\text{rel}} \rangle$ to lower values relative to the naive approximation. We compute $\langle \sigma v_{\text{rel}} \rangle$ as a function of temperature and solve the equation for the number density of thermal relic WIMPs numerically,[2] using both a full numerical integration and a very accurate approximation described in Appendix B. The two methods agree to within less than 1%.

The resulting contours of constant relic density are shown in the plane of m_S and the coupling λ_{hS} in Fig. 1. We display them both over the entire likely range of dark matter mass values (45 GeV $\leq m_S \leq$ 5 TeV) and in the region $m_S \sim m_h/2$ in which annihilation is resonantly enhanced. Constraints from the Higgs invisible width are also plotted in the low-mass region. Below $m_h/2$, the two constraints combine to rule out all but a small triangle in the m_S–λ_{hS} plane, including masses in the range 52.5–62.5 GeV. In the region above $m_h/2$, the relic density constrains the coupling as a function of mass in a way that can be approximately fit by the dependence $\log_{10}\lambda_{hS} > -3.63 + 1.04\log_{10}(m_S/\text{GeV})$. We plot up to $\lambda_{hS} \sim 8$, which is at the (generous) upper limit of where the theory can be expected to remain perturbative.

IV. INDIRECT DETECTION

Annihilation of scalar singlet DM into SM particles offers similar opportunities for indirect detection as with other WIMP DM candidates [55–59]. The strongest current limits come from gamma-ray searches for annihilation in dwarf spheroidal galaxies [60–66] (for a recent general review, see Ref. [67]) and impacts of DM annihilation at $z \sim 600$ on the

[2]We henceforth refer to this as the "Lee–Weinberg equation" with reference to Ref. [53] but note that it also appeared earlier, e.g., in Ref. [54].

angular power spectrum of the CMB [68–76]. At large WIMP masses, it is expected [77,78] that CTA will provide strong constraints.

We calculate limits on the scalar singlet parameter space implied by indirect detection using a combined likelihood function:

$$\ln \mathcal{L}_{\rm total}(m_S, \lambda_{hS}) = \ln \mathcal{L}_{\rm CMB}(m_S, \lambda_{hS}) + \ln \mathcal{L}_{\rm dwarfs}(m_S, \lambda_{hS}) + \ln \mathcal{L}_{\rm CTA}(m_S, \lambda_{hS}). \quad (7)$$

In general, $\mathcal{L}_{\rm total}$ includes components from all three indirect searches, but we only include CTA when discussing projected limits. All three likelihood functions depend in a direct sense upon m_S, but only indirectly upon λ_{hS}, via the zero-velocity annihilation cross section $\langle \sigma v_{\rm rel} \rangle_0$, the branching fractions r_i to the ith SM annihilation channel, and the total relic density.

We scale all indirect signals for the appropriate relic density for each combination of m_S and λ_{hS} self-consistently, suppressing signals where S constitutes only a fraction of the total dark matter. Where the thermal relic density of S is actually *larger* than the observed dark matter relic density, we simply rescale signals in exactly the same way, increasing the expected signals. We choose to do this rather than fix the relic density to the observed value in this region for the sake of simplicity and illustration; this region is robustly excluded anyway by the relic density constraint, and the thermal abundance could only be reduced to the observed value if some additional nonthermal effects were added to the scalar singlet theory, which would not be in the spirit of our analysis here.

We calculate $\langle \sigma v_{\rm rel} \rangle_0$ including all allowed 2-body SM final states as per Eqs. (4) and (A4) for $m_S \leq m_t$ or Eqs. (A4), (A1), and (A2) for $m_S > m_t$. To estimate r_i, we calculate $\langle \sigma v_{\rm rel} \rangle_{0,i}$ for annihilation into a given channel i using these cross sections[3] with the zero-velocity replacement $\sqrt{s} \to 2m_S$ and take $r_i = \langle \sigma v_{\rm rel} \rangle_{0,i} / \langle \sigma v_{\rm rel} \rangle_0$. For m_S just below m_W and m_Z, where $\langle \sigma v_{\rm rel} \rangle_0$ comes from the factorization approximation, we assign any remaining branching fraction to 3- and 4-body final states arising from annihilation into virtual gauge bosons corresponding to the next most massive threshold, i.e., $(W^+W^-)^*$ for $m_S < m_W$ and $(ZZ)^*$ for $m_W \leq m_S < m_Z$.

The final yields of photons and electrons from annihilation into each SM final state that we use for CMB limits come from the PPPC4DMID [79]. The gamma-ray yields we use for Fermi and CTA calculations are from DARKSUSY [80], which we supplement with the photon yield for the hh annihilation channel from PPPC4DMID.[4] For channels in common, we find good agreement between the gamma yields of PPPC4DMID and DARKSUSY.

Yields from the 3- and 4-body final states initiated by virtual gauge bosons are also required. As these are not already available, for Fermi and CTA, we estimate the photon yields by analytically extending those of the WW and ZZ channels below threshold. This is feasible because the integrated photon multiplicity per annihilation in the energy windows considered in each analysis is very close to linear with m_S. We therefore fit a straight line to this multiplicity over a few GeV above threshold in each case and use it to extrapolate a small way below threshold (< 10 GeV), in the region in which the emission of virtual gauge bosons is significant. This is an extremely good approximation for Fermi and reasonable for CTA also, although not as good as for Fermi due to the energy dependence of the CTA effective area in this region. If anything, the approximation is marginally optimistic for Fermi (in that the actual yield curve is ever so slightly concave down), whereas, for CTA, it is conservative (as the true yield curve is slightly concave up). We do not perform this exercise for CMB limits, as the actual limits near the W and Z thresholds are strongly dominated by Fermi anyway, and it would be more cumbersome to incorporate this into the CMB analysis; we hence assume that 3- and 4-body final states do not contribute anything to CMB limits, which gives a conservative limit in this region.

To show the relative importance of the various final states as a function of m_S, we plot their branching fractions in Fig. 2, along the line in $\{m_S, \lambda_{hS}\}$-space where S constitutes the entire observed relic density. Here, we combine the branching fractions of on-shell and off-shell gauge bosons.

A. CMB likelihood

We take the CMB likelihood function $\mathcal{L}_{\rm CMB}$ directly from the results presented for annihilation in Ref. [75] (which were partially based on earlier results in Refs. [73,74]), using tables of the effective fraction $f_{\rm eff}$ of the DM rest mass injected as additional energy into the primordial gas. We interpolate $f_{\rm eff}$ linearly in $\log m_S$, then use the calculated values of r_i and $\langle \sigma v \rangle_0$ for each combination of m_S and λ_{hS} to obtain the final likelihood. We extend the $f_{\rm eff}$ tables of Ref. [75] in order to accommodate S masses up to 5 TeV (see appendix C for high-mass $f_{\rm eff}$ data). For calculating current constraints, we employ the WMAP 7-year likelihood function [81]. For projected constraints, we use the Planck predictions, which assume

[3]For determining branching fractions, we simply use the tree-level versions; the QCD 1-loop correction has minimal impact above ~70 GeV, and below this, the exact partitioning into b, c, and τ has only a small effect on integrated gamma-ray yields and so modifies the overall limits from indirect detection only very slightly.

[4]For consistency with other channels, we use the hh gamma-ray yields from PPPC4DMID uncorrected for electroweak bremsstrahlung, as none of the DARKSUSY yields takes this into account; for all values of m_S we consider here, the impact of electroweak corrections on the yield from the hh channel is less than 10%.

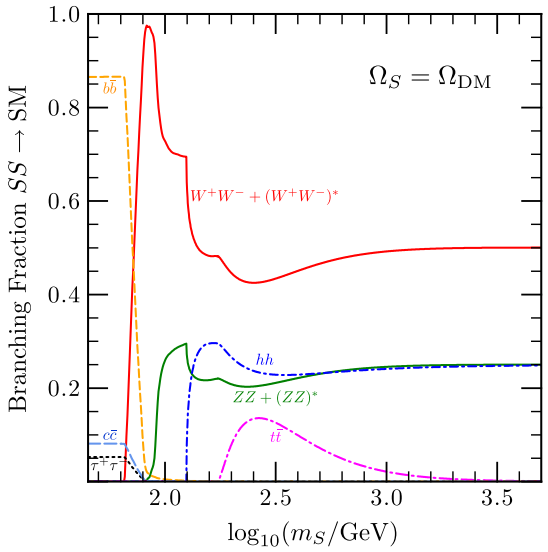

FIG. 2 (color online). Branching fractions for SS to annihilate at threshold into various SM final states vs the DM mass. We have chosen λ_{hS} at each dark matter mass such that the S relic density exactly matches the observed value; these λ_{hS} values can be seen along the $\Omega_S = \Omega_{\mathrm{DM}}$ curve in Fig. 1.

polarization data to be available. Note that, although first Planck temperature power spectrum results are available, including limits on DM annihilation [82], these are weaker than projected Planck sensitivities when polarization data is included and existing WMAP limits. A factor of a few better constraints than the WMAP7 ones we use are available from WMAP9 + SPT + ACT data [83], but this improvement will be mostly nullified by a similar degradation in the limits due to corrections to the results of Refs. [73,74], as discussed in Ref. [84].

B. Fermi dwarf likelihood

The nonobservation of gamma-ray emission from dwarf spheroidal galaxies by Fermi can be used to put strong constraints on the annihilation cross section of dark matter particles [64–66]. We calculate the corresponding Fermi dwarf likelihood function $\mathcal{L}_{\mathrm{dwarfs}}$ based on the results from Ref. [64], in which limits on the integrated dark matter signal flux with energies from 1 to 100 GeV were presented. An alternative treatment with a finer energy binning can be found in Ref. [66].

From a region $\Delta\Omega$ toward a dwarf spheroidal, one expects a differential flux of dark matter signal photons that is given by

$$\frac{\mathrm{d}\phi}{\mathrm{d}E} = \frac{\langle\sigma v_{\mathrm{rel}}\rangle}{8\pi m_S^2}\frac{\mathrm{d}N_\gamma}{\mathrm{d}E}\underbrace{\int_{\Delta\Omega}\mathrm{d}\Omega\int_{\mathrm{l.o.s.}}\mathrm{d}s\rho^2}_{\equiv J}. \tag{8}$$

Here, $\mathrm{d}N_\gamma/\mathrm{d}E$ denotes the energy distribution of photons produced per annihilation, and $\int\mathrm{d}s$ is a line-of-sight integral. The dwarf spheroidals mainly differ in their dark matter density distribution ρ and their distance from the Sun, such that the J factor has to be determined for each dwarf individually. On the other hand, the prefactor is universal.

In Ref. [64], the authors analyzed the gamma-ray flux from seven dwarf spheroidals. They determined the probability mass function of the background events in their signal regions empirically by subsampling nearby regions and found good agreement with Poisson noise. The J factors of the individual dwarfs were adopted from Ref. [65] and used to define optimized combined confidence belts that weigh the contribution from each dwarf according to the probability that observed events belong to the background. This procedure leads to a combined upper limit on the quantity $\Phi_{\mathrm{PP}} \equiv J^{-1}\int_1^{100\,\mathrm{GeV}}\mathrm{d}E\mathrm{d}\phi/\mathrm{d}E$. At 95% C.L., it reads $\Phi_{\mathrm{PP}} \leq 5.0^{+4.3}_{-4.5}\times 10^{-30}\ \mathrm{cm}^3\,\mathrm{s}^{-1}\,\mathrm{GeV}^{-2}$. The indicated errors correspond to uncertainties in the J values, which were not taken directly into account when constructing the confidence belts. Here, we adopt the central value and note that, within the quoted J value uncertainties, our limits on λ_{hs} could be weaken by up to a factor of 1.36.

Our construction of a likelihood function for Φ_{PP} works as follows. From the upper limits on Φ_{PP} as a function of the confidence level[5] α, we determine the inverse function $\alpha = \alpha(\Phi_{\mathrm{PP}})$. Roughly speaking, this function returns the probability (in repeated experiments) of measuring less than the observed number of events, given some true value of Φ_{PP}. This can be mapped onto a likelihood function,

$$-2\ln\mathcal{L}_{\mathrm{dwarfs}}(\Phi_{\mathrm{PP}}) = \mathrm{ISF}[\alpha(\Phi_{\mathrm{PP}})], \tag{9}$$

where $\mathrm{ISF}(x)$ is the inverse survival probability function of a $\chi^2_{k=1}$ distribution. In this way, we obtain $-2\ln\mathcal{L}(5.0\times 10^{-30}\ \mathrm{cm}^3\,\mathrm{s}^{-1}\,\mathrm{GeV}^{-2}) \simeq 4.0$, as expected for a 95% C.L. limit.

When deriving *projected* limits, we assume that Fermi operates for a total of at least 10 years in the current survey mode and that it is able to add a further ten new southern dwarfs to its combined search. We assume conservatively that the limits on $\langle\sigma v_{\mathrm{rel}}\rangle$ will scale as $\sqrt{N}$, following the improvement in the signal-to-noise ratio; our projected Fermi sensitivities are therefore based on rescaling the current limits by a factor of $\sqrt{20/10\times 10/3} \approx 2.68$.

C. CTA likelihood

For the CTA likelihood function $\mathcal{L}_{\mathrm{CTA}}$, we reconstruct the official CTA sensitivities for searches for dark matter annihilation toward the Galactic center [77], with a few reasonable alternative choices for different parameters. Specifically, we use the "ring method," assume an Navarro-Frenk-White [85] DM profile, 500 h of observing time, and an effective area corresponding to an extended array including both European and proposed

[5]These were kindly provided by the authors of Ref. [64].

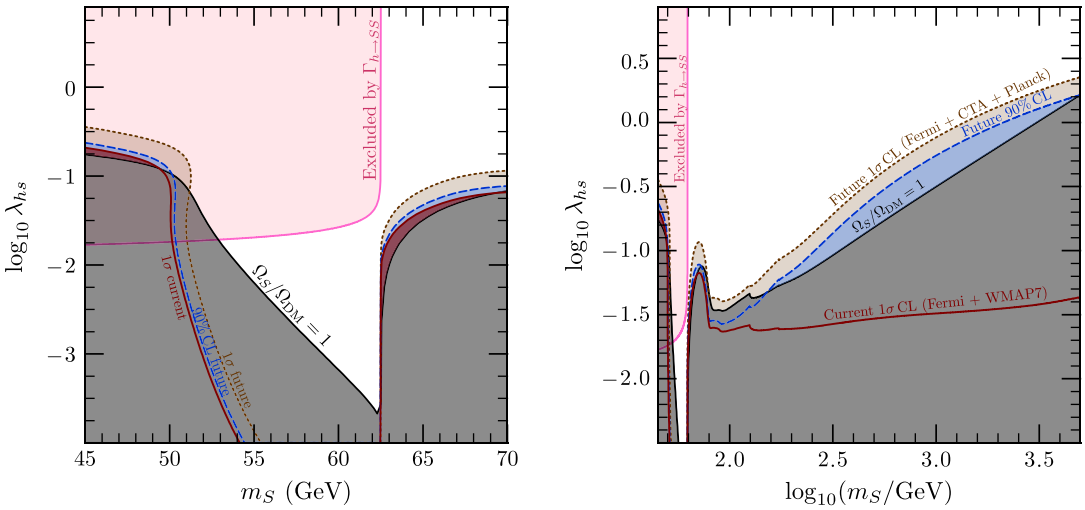

FIG. 3 (color online). Limits on scalar singlet dark matter from indirect searches for dark matter annihilation. The lowermost shaded region is ruled out because these models exceed the observed relic density. Regions below the other curves are in tension with indirect searches, or will be in the future: at more than 1σ according to current data from Fermi dwarf galaxy observations and WMAP 7-year CMB data (solid), at $\geq$90% C.L. (dashes) and $\geq 1\sigma$ C.L. (dots) with CTA, Planck polarization data, and future Fermi observations. The area ruled out by the Higgs invisible width at 2σ C.L. is indicated by the shaded region in the upper left-hand corner of both plots. Note that all indirect detection signals are scaled for the thermal relic density of the scalar singlet, regardless of whether that density is greater than or less than the observed density of dark matter. Left: a closeup of the resonant annihilation region. Right: the full mass range.

U.S. contributions [86]. We include a simple background model based on an E^{-3} electron power law in the sensitivity calculation but neglect protons and do not consider possible systematic effects in the background determination. We caution that, although neglecting background systematics leads to good agreement with recent CTA projections [78], it may result in overly optimistic sensitivities. Full details are given in Appendix D.

D. Indirect detection results

In Fig. 3, we show the combined sensitivity of indirect detection to different parts of the scalar singlet parameter space. For current limits, incorporating existing data from the Fermi combined dwarf analysis and WMAP7, we give only a 1σ band. Almost no parameter space not already excluded by relic density considerations is excluded at much higher C.L. than this. The region $m_h/2 \leq m_S \leq 70$ GeV, where S makes up all of the dark matter, can be seen to be in tension with existing indirect searches at slightly more than the 1σ level. The same is true for a small region at $m_S \leq 49$ GeV, but this is within the area already excluded by the invisible width constraint.

Future combined limits incorporating Planck polarization data, CTA, and extended Fermi dwarf observations will be able to probe the region where S is all the dark matter for $m_h/2 \leq m_S \leq 74$ GeV at 90% C.L. The absence of a signal in any of these searches will place all scalar singlet masses from $m_h/2$ to over 5 TeV in tension with indirect detection at more than the 1σ level, if S makes up all the DM. As mentioned earlier, however, CTA sensitivities should be taken with something of a grain of salt. In Fig. 4 we show the breakdown of the projected 90% C.L. limit into the three different searches. At low masses, Fermi dominates the limit, whereas above $m_S \sim m_h$, CTA takes over. The impact of neglecting 3- and

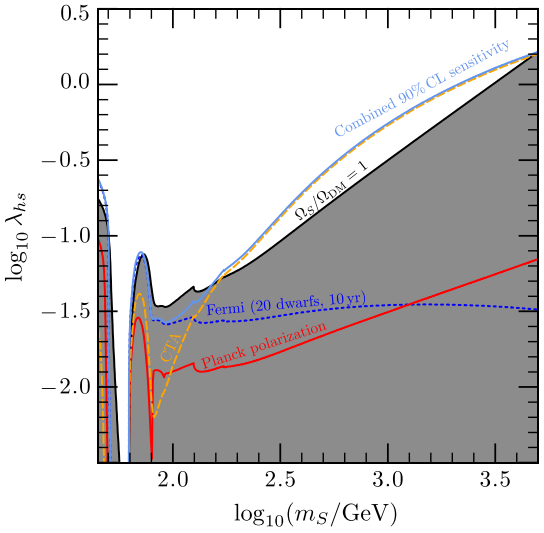

FIG. 4 (color online). Contributions of different searches for dark matter annihilation to the combined future 90% C.L. exclusion curve. The limit from future Fermi searches for annihilation in dwarf galaxies alone are shown by the dotted line, assuming 10 years of exposure and the discovery of a further ten southern dwarfs. The impact of Planck alone, including polarization data, can be seen from the solid line, and the projected impact of CTA is shown as a dashed line. The parameter space excluded by the relic density appears once more as a dark-shaded area in the lower part of the plot.

4-body final states on the CMB limit can be seen just below $m_S = m_W$ and $m_S = m_Z$, where the CMB curve takes brief downturns before recovering once the threshold is passed.

V. DIRECT DETECTION

We begin our discussion of the limits from direct searches with a fresh analysis of the complementary determinations of the Higgs-nucleon coupling, which enters in the cross section for singlet dark matter scattering on nuclei. Thanks to vigorous activity within the lattice and the theoretical communities, this coupling seems to be better determined now than it was just a few years ago. For further historical details and impacts of nuclear uncertainties on dark matter direct detection, see Refs. [87–89].

A. Higgs-nucleon coupling

In the past, one of the largest uncertainties in the analysis of singlet DM couplings to nucleons has been the Higgs-nucleon coupling, $f_N m_N/v_0$, which depends upon the quark content of the nucleon for each quark flavor. Here, $m_N = 0.946$ GeV is the nucleon mass (we ignore the small differences between neutrons and protons here). In general, f_N can be expressed in the form

$$f_N = \sum_q f_q = \sum_q \frac{m_q}{m_N}\langle N|\bar{q}q|N\rangle, \tag{10}$$

where the sum is over all quark flavors. The contributions from heavy quarks $q = c, b, t$ can be expressed in terms of the light ones,

$$\sum_{q=c,b,t} f_q = \frac{2}{9}\left(1 - \sum_{q=u,d,s} f_q\right), \tag{11}$$

by the following argument [90]. First, by equating the trace of the stress-energy tensor at low and high scales,

$$m_N \bar{N}N = \sum_q m_q \bar{q}q - (7\alpha_s/8\pi)G_{\mu\nu}G^{\mu\nu}, \tag{12}$$

and taking the nucleon matrix element, one gets the relation

$$m_N = m_N \sum_q f_q + \frac{21}{2}A, \tag{13}$$

with

$$A \equiv -\frac{1}{12\pi}\langle N|G_{\mu\nu}G^{\mu\nu}|N\rangle. \tag{14}$$

Second, $\langle N|\bar{q}q|N\rangle$ for the heavy quarks comes from the triangle diagram that generates the $hG_{\mu\nu}G^{\mu\nu}$ coupling. Therefore, the heavy-quark f_q values are related to A through $f_q = A/m_N$ for $q = c$, b, t. Eliminating A from these equations leads to the claimed relation between the heavy and light quark f_q values. From the above argument, the overall coupling is

$$f_N = \frac{2}{9} + \frac{7}{9}\sum_{q=u,d,s} f_q. \tag{15}$$

The contributions from u, d, and s are related to the light quark matrix element σ_l (which is related to the pion-nucleon isoscalar amplitude $\Sigma_{\pi N}$; see, e.g., Ref. [37]),

$$\sigma_l = m_l\langle N|\bar{u}u + \bar{d}d|N\rangle, \tag{16}$$

where $m_l \equiv \frac{1}{2}(m_u + m_d)$, and the nonsinglet combination

$$\sigma_0 = m_l\langle N|\bar{u}u + \bar{d}d - 2\bar{s}s|N\rangle \tag{17}$$

and the fairly well known isospin breaking ratio[6]

$$z = \frac{\langle N|\bar{u}u - \bar{s}s|N\rangle}{\langle N|\bar{d}d - \bar{s}s|N\rangle} \approx 1.49. \tag{18}$$

In principle, these relations suffice to determine all light quark f_q values. Indeed, if we further define the strangeness content through the ratio

$$y = \frac{2\langle N|\bar{s}s|N\rangle}{\langle N|\bar{u}u + \bar{d}d|N\rangle} = 1 - \frac{\sigma_0}{\sigma_l}, \tag{19}$$

we can solve

$$\begin{aligned} f_u &= \frac{m_u}{m_u + m_d}\frac{\sigma_l}{m_N}\frac{2z + y(1-z)}{1+z}, \\ f_d &= \frac{m_d}{m_u + m_d}\frac{\sigma_l}{m_N}\frac{2 - y(1-z)}{1+z}, \\ f_s &= \frac{m_S}{m_u + m_d}\frac{\sigma_l}{m_N}y. \end{aligned} \tag{20}$$

The quantities σ_l and σ_0 have been evaluated by chiral perturbation theory (ChPT), pion-nucleon scattering, and lattice simulations, with some scatter in the results. For a long time, the canonical ChPT value of σ_0 was $\sigma_0 \approx 35 \pm 7$ MeV [41–43], but a recent computation found $\sigma_0 \approx 58 \pm 9$ MeV [44]. Similarly, for σ_l, the older perturbation theory result was $\sigma_l \approx 45$ MeV, whereas Ref. [45] found $\sigma_l = 59 \pm 7$ MeV. The new result is in good agreement with partial wave analysis of pion-nucleon scattering ($\sigma_l = 64 \pm 8$ MeV [46]) and in particular with a recent lattice evaluation ($\sigma_l = 58 \pm 9$ MeV [40]). Depending on which of these sets one accepts, there is a wide range of possible strangeness contents of the nucleon. Fortunately, there also exist many recent, direct lattice evaluations of the strangeness matrix element,

$$\sigma_s = m_s\langle N|\bar{s}s|N\rangle, \tag{21}$$

using $2 + 1$ dynamical quark flavors [30–40]. For a recent review, see Ref. [37]. Although there still is some scatter also in these results, all evaluations agree that σ_s is quite small. Based on a subset of more constraining studies, Refs. [36,47] reported world averages of $\sigma_s = 43 \pm 8$ MeV

[6]This corrects a typo in the definition of z given in Ref. [25].

and $\sigma_s = 40 \pm 10$ MeV, respectively. However, Ref. [37] arrived at a looser result, $\sigma_s = 40 \pm 30$ MeV, by including also less constraining results in the analysis. (The difference between different sets may be associated with taking the correct continuum limit.)

We have made a statistical analysis of what f_N might be in light of these constraints on the nucleon matrix elements. We choose to use the isospin breaking ratio z (Eq. (18)) and the lattice determinations for σ_l and σ_s as inputs. We choose σ_l because there is a consensus on its value when evaluated three different ways and σ_s because lattice simulations agree in the prediction that it is small. To be precise, we shall use a fixed value for isospin breaking $z = 1.49$ and $\sigma_l = 58 \pm 9$ MeV with a Gaussian distribution. For σ_s, we explore two possibilities: either $\sigma_s = 43 \pm 8$ MeV with a Gaussian distribution or $\sigma_s < 70$ MeV with a top-hat distribution. In addition, we allow the light quark masses to be Gaussian distributed with $m_q = m_{q,0} \pm \delta m_q$ with $\delta m_q \equiv \frac{1}{2}(\delta m_{q+} + \delta m_{q-})$, where [47]

$$\begin{array}{lll} m_{u,0} = 2.5 & \delta m_{u,+} = 0.6 & \delta m_{u,-} = 0.8 \\ m_{d,0} = 5 & \delta m_{d,+} = 0.7 & \delta m_{d,-} = 0.9 \\ m_{s,0} = 100 & \delta m_{s,+} = 30 & \delta m_{s,-} = 20. \end{array} \quad (22)$$

Here, all units are in MeV. Finally, the nucleon mass is $m_N = (m_n + m_p)/2 = 938.95$ MeV.

With these inputs, we generate 10^7 random realizations, from which we construct the distributions for the strangeness content y, the matrix element σ_0, and finally f_N. Results are displayed in Fig. 5. Note that σ_0 distribution is a prediction here. It is satisfying to see that it does not depend much on the strangeness input, and that the distribution ($\sigma_0 = 55 \pm 9$ MeV) agrees very well with the recent ChPT calculation [44]. This lends support to the self-consistency of our analysis. The strangeness content y mostly reflects the input choices; the top-hat choice assumes only an upper bound for the strangeness matrix element, so y is only restricted from above. This upper bound is almost the same as the upper bound in the Gaussian case, which is not consistent with $y = 0$. However, what interests us is that both strangeness input choices give comparable, almost Gaussian, distributions for the Higgs-nucleon coupling. In the top-hat case, we find $f_N = 0.341 \pm 0.021$, and in the Gaussian case, $f_N = 0.348 \pm 0.015$. All uncertainties quoted are formal 1-σ (68.3% C.L.) limits.

Thus, the error in the determination of f_N is quite a lot smaller than one might believe—less than 10% according to our analysis. Taking the mean value of the two different strangeness input choices, we will use $f_N = 0.345$ in our analysis. This is also exactly the central value that we would have obtained (with an uncertainty of 0.016) had we instead used $\sigma_s = 40 \pm 10$ MeV, as advocated in Ref. [36].

B. Direct detection limits

The cross section for spin-independent scattering of singlet DM on nucleons is given by

$$\sigma_{\rm SI} = \frac{\lambda_{hS}^2 f_N^2}{4\pi} \frac{\mu^2 m_n^2}{m_h^4 m_S^2}, \quad (23)$$

where $\mu = m_n m_S/(m_n + m_S)$ is the DM-nucleon reduced mass. The current best limit on $\sigma_{\rm SI}$ comes from the XENON100 experiment [29]. In our analysis, we allow for the singlet to provide a fraction of the total dark matter, as indicated by the contours in Fig. 1. We thus apply the 90% C.L. limits of Ref. [29] (which assume a local DM density of 0.3 GeV cm^{-3}), appropriately weighted by the fraction of dark matter in the singlet component.

In the standard analysis in which only a single component of DM with the full relic density is assumed, the differential rate of detection dR/dE is proportional to $(\rho_\odot/m_{\rm DM})\sigma_{\rm SI}$, where $\rho_\odot$ is the local DM mass density. Thus, the appropriate rescaling of the limiting value of $\sigma_{\rm SI}$ is by the fraction $f_{\rm rel} = \Omega_S/\Omega_{\rm DM}$ of energy density contributed by S to the total DM density. We assume that there is no difference in the clustering properties of the singlet component and the dominant component so that the local energy density of S is $f_{\rm rel}\rho_\odot$. We therefore demand for every value of $\{\lambda_{hS}, m_S\}$ that

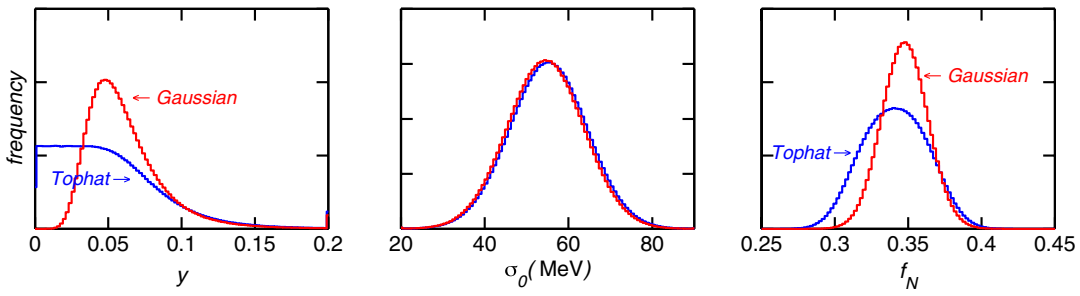

FIG. 5 (color online). Predicted distributions (in arbitrary units) of the strangeness content y of the nucleon (left), the nucleon matrix element σ_0 (center), and the Higgs-nucleon coupling factor f_N (right). These are drawn from a random sample generated using experimental and theoretical constraints, as explained in the text.

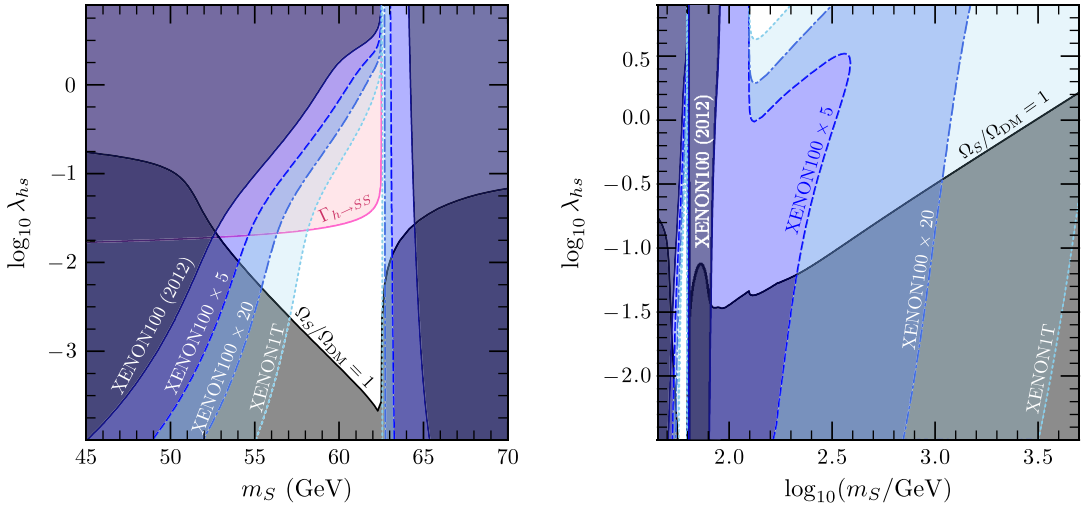

FIG. 6 (color online). Limits from direct detection on the parameter space of scalar singlet dark matter. The areas excluded by present limits from XENON100 are delineated with near-vertical solid lines and dark shading (not to be confused with the diagonal solid line and corresponding dark shading indicating the relic density bound). Dashed, dotted, and dotted-dashed lines indicate the areas that will be probed by future direct detection experiments, assuming 5 times the sensitivity of XENON100 (dashes, medium-dark shading), 20 times (dotted-dashed line, medium-light shading), and 100 times, corresponding to XENON 1-ton (dots, light shading). Note that all direct detection signals are scaled for the thermal relic density of the scalar singlet, regardless of whether that density is greater than or less than the observed density of dark matter. Left: a closeup of the resonant annihilation region, with the area ruled out by the Higgs invisible width at 2σ C.L. indicated by the shaded region in the upper left-hand corner. Right: the full mass range.

$$\sigma_{\text{eff}} \equiv f_{\text{rel}}\sigma_{\text{SI}} \leq \sigma_{\text{Xe}}, \tag{24}$$

where σ_{Xe} is the 90% C.L. limit from XENON100. As with indirect signals, for simplicity, we perform the same rescaling even if the thermal relic density exceeds the observed value.

The resulting constraints in the m_S–λ_{hS} plane are shown in Fig. 6 as well as projections for how these limits will improve in future xenon-based experiments, assuming that the sensitivity as a function of mass scales relative to that of XENON100 simply by the exposure. The contours showing improvements in the current sensitivity by a factor of 5 or 20 will be relevant in the coming year as LUX expects to achieve such values [91,92], while XENON1T projects a factor of 100 improvement [93,94] within two years. The left panel of Fig. 6 focuses on the resonant annihilation region $m_S \sim m_h/2$, showing that a small triangle of parameter space will continue to be allowed for m_S between $m_h/2$ and ~58 GeV. Values below 53 GeV are already robustly excluded, making it highly unlikely that singlet dark matter can explain various hints of direct detection that have been seen at low masses ~10 GeV [95,96].

On the high-mass side, the right panel of Fig. 6 implies that most of the relevant remaining parameter space will be ruled out in the next few years. In particular, XENON1T will be able to exclude masses up to 7 TeV, for which the coupling must be rather large, $\lambda_{hS} > 2.4$, leaving little theoretical room for this model if it is not discovered.

Naively, one might expect the contours of direct detection sensitivity in the high-m_S regions to be exactly vertical in Fig. 6 rather than being slightly inclined. This is because $f_{\text{eff}} \sim \langle\sigma v_{\text{rel}}\rangle^{-1} \sim (m_S/\lambda_{hS})^2$ in Eq. (24), which is exactly inverse to σ_{SI}.[7] According to this argument, the direct detection sensitivity would be independent of λ_{hS} and only scale inversely with m_S due to the DM number density going as $1/m_S$. However, this is not exactly right because the DM relic density has an additional weak logarithmic dependence on $\langle\sigma v_{\text{rel}}\rangle$ through the freeze-out temperature, leading to the relation [see Eqs. (B7) and (B8)], with the approximation $A_f \cong x_f Z_f$),

$$f_{\text{rel}} \sim (x_f A_f)^{-1} \sim \frac{\ln(c m_S \langle\sigma v_{\text{rel}}\rangle)}{m_S\langle\sigma v_{\text{rel}}\rangle} \sim (m_S\langle\sigma v_{\text{rel}}\rangle)^{-1+\epsilon}, \tag{25}$$

for some constant c and a small fractional power ϵ, which we find to be $\epsilon \cong 0.05$. Taylor expanding the last expression in ϵ produces the log in the numerator.

The shape of the exclusion contours in the m_S–λ_{hS} plane of course carries over into a similar shape in the m_S–σ_{SI} plane, which is the more customary one for direct detection constraints. We nevertheless replot them in this form in Fig. 7 to emphasize that they look very different

[7]There is some additional dependence upon λ_{hS} in the annihilation cross section for $SS \to hh$, but this is very weak at large m_S.

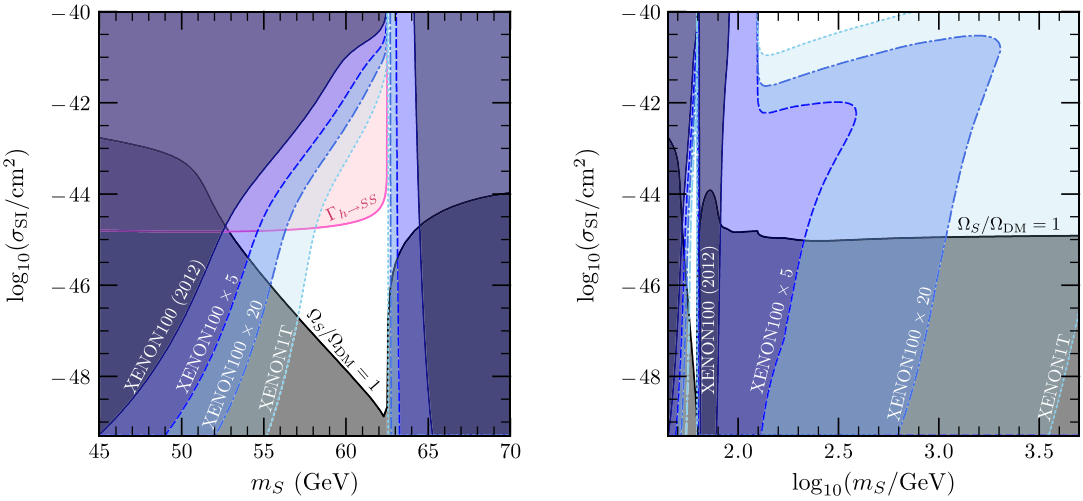

FIG. 7 (color online). Limits from direct detection on scalar singlet dark matter, shown in the familiar mass–cross section plane. Areas excluded by XENON100, future experiments, and the relic density are as per Fig. 6. The unusual shapes of the curves compared to traditional direct detection constraint plots is due to our self-consistent treatment of subdominant relic densities. Note that all direct detection signals are scaled for the thermal relic density of the scalar singlet, regardless of whether that density is greater than or less than the observed density of dark matter. Left: a closeup of the resonant annihilation region, with the area ruled out by the Higgs invisible width at 2σ C.L. indicated by the shaded region in the upper left-hand corner. Right: the full mass range.

from the usual ones, being mostly vertical rather than horizontal. Normally, the DM relic density is assumed to take the standard value because the annihilation cross section $\langle\sigma v_{\rm rel}\rangle$ that sets $\Omega_{\rm DM}$ is distinct from that for detection, $\sigma_{\rm SI}$. Only because they are so closely related in the present model do we get limits that are modified by the changing relic density as one scans the parameter space.

VI. APPLICATIONS

The singlet model we have considered, or modest elaborations of it, has implications for a number of purposes other than just explaining the dark matter or one of its components. These include strengthening the electroweak phase transition, explaining tentative evidence for 130 GeV and continuum gamma rays from the Galactic center, hints of an extra component of dark radiation from analysis of the cosmic microwave background, a candidate for the curvaton mechanism, and impacting the stability of the Higgs potential near the Planck scale. We briefly discuss these issues in the present section.

A. Strong electroweak phase transition

Recently, it was pointed out that a strong electroweak phase transition (EWPT), with $v_c/T_c \geq 1$ at the critical temperature, can be obtained in the scalar singlet dark matter model if $\lambda_{hS} \gtrsim 0.1$ [49], thus requiring the singlet to comprise a subdominant component of the total dark matter density. The criterion $v_c/T_c > 1$ is needed for a successful model of electroweak baryogenesis (also considered in Ref. [49]). The effect of the singlet on the EWPT depends upon an additional operator $\lambda_S S^4$, which was not relevant for the preceding analysis. By scanning over λ_S, Ref. [49] produced many random realizations of models giving a strong enough EWPT. Here, we have repeated this procedure in order to display the range of viable models in the space of $\{m_S, \lambda_{hS}\}$ for comparison with Figs. 1–7.

In these models, the Z_2 symmetry $S \to -S$ is temporarily broken by a VEV, S_c, at the critical temperature. It is convenient to parametrize the S^4 coupling as $\lambda_S = (\lambda_h/4)(v_c/S_c)^4$, where $\lambda_h = 0.13$ is the Higgs quartic coupling. We consider $(v_c/S_c)^4$ in the range 0.1–10, corresponding to $\lambda_S \in [3 \times 10^{-4}, 3]$. The results are shown in Fig. 8. In the left panel, shaded bands of models correspond to intervals of v_c/S_c as shown in the key of the figure; larger v_c/S_c corresponds to larger λ_{hS} at a given mass m_S. There is an island of small λ_{hS} near $m_S \sim m_h/2$ where SS annihilations are resonantly enhanced. These correspond to $v_c/S_c < 1$. In the right panel, we take several discrete values of v_c/S_c to better illustrate the dependence of v_c/T_c on the parameters m_S, λ_{hS}. For a given value of v_c/S_c, there is always a maximum mass m_S beyond which there is no longer a strong phase transition. For large v_c/S_c, this occurs at strong couplings $\lambda_{hS} > 5$ that we do not consider.

Contours showing the current direct detection limit [29] and projected ones for experiments with 5 and 20 times greater sensitivity are also shown in the right panel of Fig. 8. A large region of the remaining parameter space

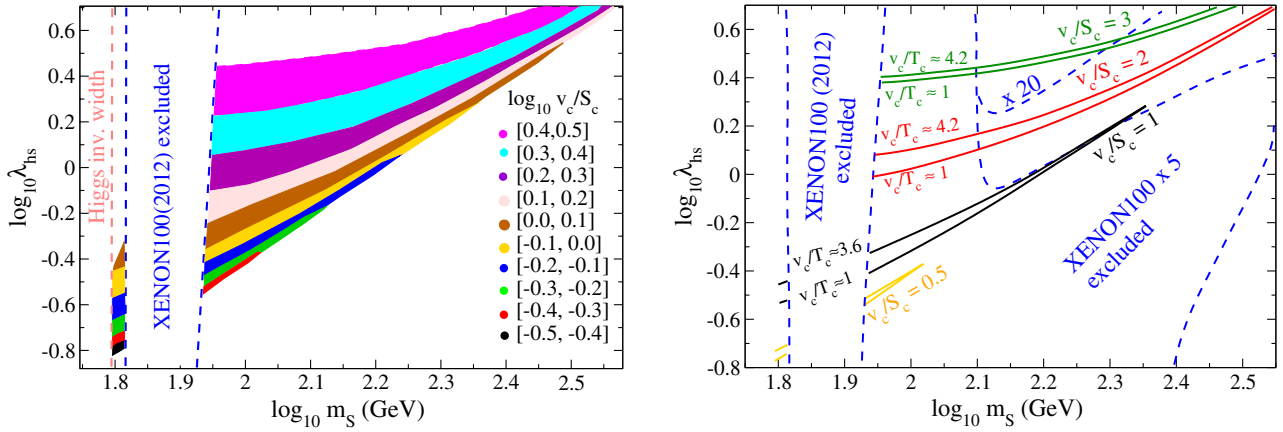

FIG. 8 (color online). Left: bands of models having a strong enough electroweak phase transition for electroweak baryogenesis, scanning over the ratio of VEVs at the critical temperature, v_c/S_c. Different shades correspond to intervals of $\log_{10} v_c/S_c$ shown in the key, with lowest values occurring lower on the plot. Right: similar plot for fixed values of $v_c/S_c = 0.5$, 1, 2, 3 and v_c/T_c close to 1 or to its maximum value, for the given v_c/S_c. Excluded regions for XENON100 (2012) and for future experiments with 5 and 20 times greater sensitivity are shown. The excluded region $m_S < m_h/2$ from the invisible Higgs width constraint is shown on the left sides of both plots.

will be excluded by the LUX experiment [91,92], which plans to achieve a factor of better than 10 times improvement relative to Ref. [29] by the end of 2013. Within two years, XENON1T expects to reach 100 times the sensitivity of the XENON100 (2012) [93,94].

The island of models near $m_S \sim m_h/2$ is squeezed on the left by the requirement $m_S > m_h/2$ due to the constraint on the invisible width of the Higgs and on the right by the direct detection bound. This region will become increasingly narrow as the XENON bounds improve, as shown close up in Fig. 9.

B. 130 GeV gamma-ray line

There has been significant interest in tentative evidence for a 130 GeV gamma-ray line from the Galactic center found in Fermi-LAT data [97–104], which might be interpreted as coming from annihilation of dark matter. In Ref. [105], it was suggested that the scalar singlet dark matter model could provide an explanation, if one added an additional interaction $\lambda_{S\sigma} S^2|\sigma|^2$ with a charge-two singlet σ, transforming in the fundamental representation of a new SU(N) gauge interaction. Then, SS can annihilate into $\gamma\gamma$ through a virtual loop of σ, producing gamma rays of the observed energy if $m_S = 130$ GeV.

To get a large enough cross section into photons, S should be the dominant dark matter particle; hence, λ_{hS} should be close to 0.05. From the right panel of Fig. 6 and the previous discussion, it is clear that these values will be probed in the coming year by LUX. This conclusion could be evaded if glueballs of the new SU(N) are lighter than 130 GeV, however; in that case, λ_{hS} could be much less than 0.05 to evade the direct detection limit, while the S relic density could be achieved by annihilation of SS into glueballs, via the σ loop.

C. Continuum gamma rays from the Galactic center

An excess of continuum gamma rays has also been claimed in Fermi-LAT data toward the Galactic center [106–109]. This has been interpreted as consistent with the annihilation of dark matter with a mass of 30–50 GeV and a cross section of $\langle \sigma v_{\rm rel} \rangle_0 \sim 6\text{–}8 \times 10^{-27}$ cm^3 s^{-1}

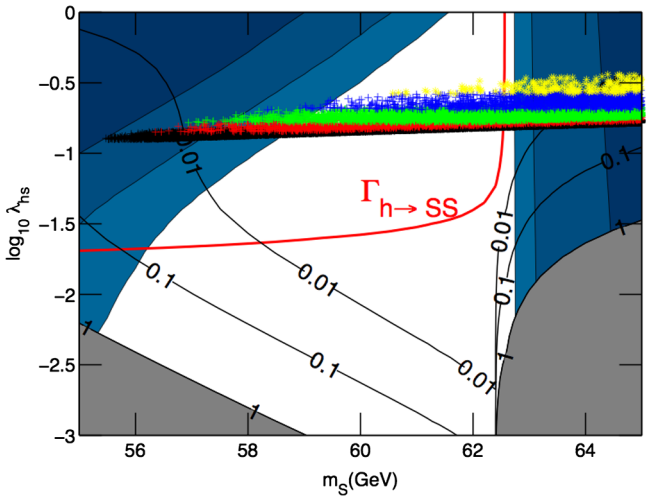

FIG. 9 (color online). Scatter plot of models with strong EWPT, focusing on the low-mass region near $m_h/2$. Shading of points follows Fig. 8. Limits from XENON100, and from future experiments with 5 and 20× greater sensitivity, are shown as vertical lines to the right of the plot and diagonal lines to the left, with the ruled out areas marked by graded (blue) shading. The area ruled out by the Higgs invisible width at 2σ C.L. lies above and to the left of the line labelled "$\Gamma_{h\to SS}$." The area ruled out by the relic density constraint is shown as usual as a dark shaded region at the bottom of the plot, with additional labelled contours indicating lines of constant subdominant relic density.

into b quarks [107,109]. Considering that the Fermi-LAT dwarf limit on annihilation into $b\bar{b}$ is $\langle\sigma v_{\rm rel}\rangle_0 \leq 4\times10^{-26}$ cm^3 s^{-1} at a mass of 50 GeV [64,65], and remembering that $\sigma v_{\rm rel}$ scales roughly as λ_{hS}^2 for fixed m_S, we see that all models that could approximately fit this signal (i.e., with appropriate cross sections and masses below ~60 GeV) lie less than 1 order of magnitude above the indirect limit shown in Fig. 3. At low masses, all these models are therefore excluded by the Higgs invisible width, and above 53 GeV, their thermal relic densities all grossly exceed the observed cosmological abundance of dark matter. Scalar singlet dark matter therefore cannot be responsible for the observed continuum gamma rays at the Galactic centre unless the theory is supplemented by some additional physics that would suppress the thermal relic density.

D. Complex singlet dark matter

Another natural generalization of scalar singlet dark matter is the case in which S is a complex scalar. With no additional interactions, this would be equivalent to two real singlets, and the potential is most naturally written in the form

$$V = \mu_S^2|S|^2 + \lambda_{hS}|S|^2|H|^2, \tag{26}$$

with $S = (S_1 + iS_2)/\sqrt{2}$ giving the relation to the canonically normalized real singlets $S_{1,2}$. The relic density n would thus be doubled relative to the real singlet model with the same values of m_S and λ_{hS}, and since n scales as $1/\langle\sigma v_{\rm rel}\rangle \sim \lambda_{hS}^{-2}$, our relic density contours would thus move upward by $\delta\log_{10}\lambda_{hS} \cong 0.15$. The direct detection signal scales roughly as N/m_S for N components of degenerate dark matter, so the contours for direct detection would move to the right by $\delta\log_{10}m_S \cong 0.3$.

It was recently suggested that hints from the CMB of an extra component of dark radiation could be explained in the context of fermionic singlet dark matter if the U(1) symmetry $\psi \to e^{i\alpha}\psi$ for dark matter number conservation is spontaneously broken near the weak scale. This leads to Nambu–Goldstone bosons comprising the dark radiation and a small mass splitting between the two dark matter components [110]. Scalar singlet dark matter as we consider here offers an alternative implementation of this idea; by adding an extra scalar X that carries dark matter charge 1 or 2 and for which the potential gives it a VEV, we can achieve a similar result. We leave the details for future investigation.

E. Curvaton model

The same model as we are studying as a dark matter candidate was recently considered as a curvaton candidate in Ref. [111]. The curvaton is a massive field for which the fluctuations during inflation later come to dominate the universe, before they decay and produce the primordial density fluctuations. This is an interesting alternative to inflaton fluctuations in the case in which the latter are subdominant. In the present model, S cannot decay, but its annihilations through resonant preheating can convert its fluctuations into Higgs particles which then decay into other standard model particles.

The region of interest in the parameter space $\{m_S, \lambda_{hS}\}$ considered by Ref. [111] is $m_S \in [10^2, 10^{11}]$ GeV, $\lambda_{hS} \in 2\times[10^{-2}, 10^{-30}]$, which, according to our analysis, should be entirely ruled out. However, we have assumed that the dark matter thermalizes at high temperatures and freezes out in the standard way, whereas the curvaton decay process is a nonthermal one, which can only be reliably calculated until the not-too-late stages of preheating. If the universe thermalizes in this scenario to a maximum temperature below the standard freeze-out value for the dark matter, then it is possible that S could be the curvaton and evade our constraints, while possibly even attaining the right relic density through this nonthermal mechanism. However, it would be numerically very challenging to test the scenario given the current limitations of lattice codes for preheating.

F. Higgs potential stability

A curious feature of the recently determined value of the Higgs boson mass is that it is slightly below what would be needed to maintain positivity of the quartic Higgs coupling λ_h under renormalization group running up to the Planck scale assuming only the standard model [112]. The top quark gives a large negative contribution to the running of λ_h, which is not quite offset by the positive contribution from λ_h itself. However, the coupling λ_{hS} gives an additional positive contribution that has the potential to bring about stability of λ_h. This effect was previously studied in Refs. [13,113–115].

Although higher-order corrections are needed to make an accurate prediction, one can reasonably approximate the size of the effect using the 1-loop contributions to the beta function β_{λ_h} in order to make a rough estimate of the magnitude of λ_{hS} needed in order to have an impact on the vacuum stability question. It was shown in Ref. [112] that a shift in the top quark mass $\delta m_t = -2$ GeV would be sufficient to yield positivity of λ_h up to the Planck scale for $m_h = 125$ GeV. This corresponds to a shift in β_{λ_h} of [116]

$$\delta\beta_{\lambda_h} = -24\frac{\delta m_t}{m_t}\frac{y_t^3}{16\pi^2} \cong \frac{0.28}{16\pi^2}, \tag{27}$$

where y_t is the top quark Yukawa coupling. On the other hand, the scalar singlet contributes an amount

$$\delta\beta_{\lambda_h} = \frac{\frac{1}{2}\lambda_{hS}^2}{16\pi^2}. \tag{28}$$

According to this estimate, values near $\lambda_{hS} \sim 0.75$ could be sufficient to achieve stability of the Higgs potential, which would correspond to DM masses $m_S \sim 3$ TeV.

The previous argument ignores the effect of the $\lambda_S S^4$ coupling on the running of λ_h, which was shown in Ref. [113] to reduce the effectiveness of λ_{hS} for improving vacuum stability. Inspection of their results (see Fig. 1 of Ref. [113]) confirms the above estimate for the needed size of $\lambda_{hS} \sim 0.75$.

VII. CONCLUSIONS

The model of scalar singlet dark matter S was proposed at least 28 years ago. We have reconsidered the prospects for its discovery by direct or indirect signals and found that the next 2 years are likely to be crucial. In particular, the XENON1T experiment should discover or rule out the scalar singlet for most reasonable values of its mass and coupling λ_{hS} to the Higgs, leaving only values $\lambda_{hS} > 2.4$ that start to be nonperturbative. We find that, in a small range of masses $m_S \sim 55$–62.5 GeV and couplings $-2 \gtrsim \log_{10}\lambda_{sh} \gtrsim -3.5$, the singlet scalar DM cannot be ruled out by any of the forthcoming observations. However, in this region, our momentum-independent relic density calculation, which solves only for the abundance rather than the DM distribution function, should be verified by use of a full momentum-dependent Boltzmann code. We argued that the theoretical uncertainty in the Higgs-nucleon coupling, which has long affected predictions, is now significantly smaller than it was until only rather recently.

If the model is excluded by direct searches, then constraints from indirect detection will no longer be competitive, but the situation will be more interesting if there is a direct detection. In that case, complementary information will be required to see whether the singlet model is preferred over other possible models. We have shown (Fig. 4) that there is a region of parameter space in which S provides a not-too-small fraction of the total dark matter while still giving an observable signal in gamma rays that might be detected by the Čerenkov Telescope Array. Interestingly, this includes a theoretically motivated region where the singlet's effect on the running of the Higgs self-coupling λ_h could push it back to a positive value at the Planck scale.

Unfortunately, for most values of the mass m_S, there is typically a rather large range of values of its coupling λ_{hS} to the Higgs for which direct detection, but not indirect detection, would be possible. These include the regions in which S could help to induce a strong electroweak phase transition. The prospects for indirect detection would be dramatically improved if S couples to some new charged particles, which has been suggested as a scenario for explaining hints of 130 GeV dark matter annihilating into gamma rays at the Galactic center. This intriguing possibility, too, will be settled in the near future, both by improvements in direct detection sensitivity and imminent observations by the HESS-II experiment [117].

ACKNOWLEDGMENTS

We thank Alex Geringer-Sameth for kindly providing his results from Ref. [64] at arbitrary confidence levels and Jan Conrad and Jenny Siegal-Gaskins for helpful discussions on CTA. J. C. is supported by the Natural Science and Engineering Research Council of Canada (NSERC) and thanks the University of Jyväskylä Physics Department for its hospitality while this work was being completed. P. S. is supported by the Banting program, administered by NSERC.

APPENDIX A: s-DEPENDENT CROSS SECTIONS

As explained in the main text, we cannot use Eq. (4) with the tabulated values of Ref. [51] for Higgs boson widths $\sqrt{s} \gtrsim 300$ GeV. Instead, we have to use the perturbative cross sections for annihilation into kinematically open channels, which are dominated by the gauge bosons and the top quark. The cross section into gauge bosons is

$$v_{\rm rel}\sigma_{\rm VV} = \frac{\lambda_{hs}^2 s}{8\pi}\delta_V v_V |D_h(s)|^2(1 - 4x + 12x^2), \quad \text{(A1)}$$

where $x \equiv M_V^2/s$, $v_{\rm V} = \sqrt{1-4x}$, $\delta_W = 1$, $\delta_Z = \frac{1}{2}$, and $|D_h(s)|^2$ is defined in Eq. (5). Annihilation into fermion final states is given by

$$v_{\rm rel}\sigma_{\rm f\bar{f}} = \frac{\lambda_{hs}^2 m_{\rm f}^2}{4\pi} X_{\rm f} v_{\rm f}^3 |D_h(s)|^2, \quad \text{(A2)}$$

where $v_{\rm f} = \sqrt{1 - 4m_{\rm f}^2/s}$ and $X_{\rm f} = 1$ for leptons, while, for quarks, it incorporates a color factor of 3 and an important 1-loop QCD correction [118]:

$$X_q = 3\left[1 + \left(\frac{3}{2}\log\frac{m_q^2}{s} + \frac{9}{4}\right)\frac{4\alpha_s}{3\pi}\right], \quad \text{(A3)}$$

where α_s is the strong coupling for which we take the value $\alpha_s = 0.12$. Using QCD-corrected annihilation rates for light quarks is an excellent approximation below the lower limit $\sqrt{s} = 90$ GeV to which Ref. [51] gives tabulated results. Neglecting QCD corrections, there would lead to an error of order $\mathcal{O}(1)$. Of course, this region turns out to be ruled out. In the large mass region, the QCD correction on the top-quark final state is quite small.

Finally, the annihilation cross section to the Higgs boson pairs is given by

$$\begin{aligned} v_{\rm rel}\sigma_{hh} = \frac{\lambda_{hs}^2}{16\pi s^2 v_S}\Bigg[&(a_R^2 + a_I^2) s v_S v_h \\ &+ 4\lambda_{sh} v_0^2 \left(a_R - \frac{\lambda_{sh} v_0^2}{s - 2m_h^2}\right)\log\left|\frac{m_S^2 - t_+}{m_S^2 - t_-}\right| \\ &+ \frac{2\lambda_{sh}^2 v_0^4 s v_S v_h}{(m_S^2 - t_-)(m_S^2 - t_+)}\Bigg], \end{aligned} \quad \text{(A4)}$$

where $v_i = \sqrt{1 - 4m_i^2/s}$, $t_\pm = m_S^2 + m_h^2 - \frac{1}{2}s(1 \mp v_S v_h)$, and

$$a_R \equiv 1 + 3m_h^2(s - m_h^2)|D_h(s)|^2$$
$$a_I \equiv 3m_h^2\sqrt{s}\Gamma_h(m_h)|D_h(s)|^2. \tag{A5}$$

In the zero-velocity limit $\sqrt{s} = 2m_S$, this cross section immediately reduces to the expression given in Eq. (4.1) of Ref. [49].

APPENDIX B: SOLUTION OF THE BOLTZMANN EQUATION

The Lee–Weinberg equation for the number density can be written as

$$\frac{dY}{dx} = Z(x)[Y_{\rm eq}^2(x) - Y^2(x)], \tag{B1}$$

where $Y \equiv n/s$ is the ratio of the WIMP number density n to entropy s, $x \equiv m/T$, and

$$Z(x) \equiv \sqrt{\frac{\pi}{45}}\frac{m_S M_{\rm Pl}}{x^2}[\sqrt{g_*}\langle v_{\rm rel}\sigma\rangle](x), \tag{B2}$$

where the average cross section $\langle v_{\rm rel}\sigma\rangle$ is given in Eq. (6) and

$$\sqrt{g_*} \equiv \frac{h_{\rm eff}}{\sqrt{g_{\rm eff}}}\left(1 + \frac{T}{3h_{\rm eff}}\frac{dh_{\rm eff}}{dT}\right), \tag{B3}$$

where $h_{\rm eff}$ and $g_{\rm eff}$ are the effective entropy and energy degrees of freedom, which we compute assuming standard model particle content. Finally,

$$Y_{\rm eq}(x) = \frac{45}{4\pi^4}\frac{x^2}{h_{\rm eff}(T)}K_2(x) \tag{B4}$$

in the Maxwell–Boltzmann approximation. We solve Eq. (B1) both numerically and in a semianalytic freeze-out approximation, which differs slightly from the one usually presented in the literature [52,119]. For a similar treatment, see, however, Ref. [120]. We begin by defining $Y \equiv (1 + \delta)Y_{\rm eq}$ and rewriting the Lee–Weinberg equation as an equation for δ:

$$\frac{d\delta}{dx} + (1 + \delta)\frac{d\log Y_{\rm eq}}{dx} = -Z(x)Y_{\rm eq}(x)\delta(\delta + 2). \tag{B5}$$

The freeze-out approximation is based on the observation that δ starts to grow slowly, such that $d\delta/dx \ll \delta$ until $\delta \sim \mathcal{O}(1)$.[8] When this holds, one can neglect the δ derivative and reduce Eq. (B5) into an algebraic equation for $\delta = \delta(x)$. We turn this argument around by assuming that the approximation holds until some freeze-out value $\delta_{\rm f}$ and solve the corresponding freeze-out $x_{\rm f} = x(\delta_{\rm f})$ from the ensuing condition:

[8]Note that, due to the leading exponential behavior at large x, $d\log Y_{\rm eq}/dx \approx -1$.

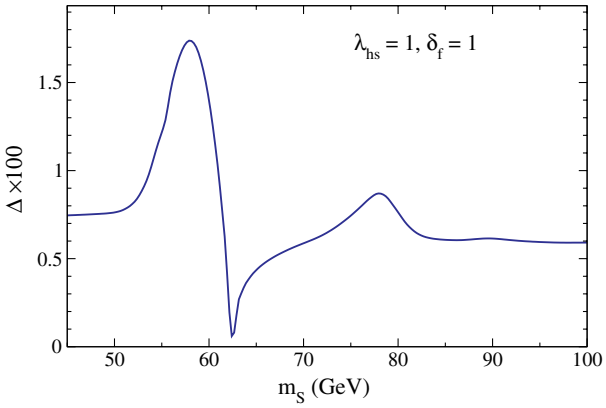

FIG. 10 (color online). Shown is the relative difference $\Delta \equiv (Y_{\rm today}^{\rm full} - Y_{\rm today})/Y_{\rm today}$, where $Y_{\rm today}$ is obtained from Eq. (B7) and $Y_{\rm today}^{\rm full}$ from a direct numerical integration of the Lee–Weinberg equation.

$$x_{\rm f} = \log\left(\frac{\delta_{\rm f}(2 + \delta_{\rm f})}{1 + \delta_{\rm f}}\frac{Z\hat{Y}_{\rm eq}^2}{\hat{Y}_{\rm eq} - \frac{d\hat{Y}_{\rm eq}}{dx}}\right)_{x_{\rm f}}, \tag{B6}$$

where $\hat{Y}_{\rm eq} \equiv e^x Y_{\rm eq}$. Equation (B6) is simple to solve by iteration. At $x = x_f$, one then has $Y_{\rm f} = (1 + \delta_{\rm f})Y_{\rm eq}(x_{\rm f})$. For $x > x_{\rm f}$, one may safely neglect the $Y_{\rm eq}^2$ term (back-reaction), which allows us to integrate the equation exactly to the final result,

$$Y_{\rm today} = \frac{Y_{\rm f}}{1 + Y_{\rm f}A_{\rm f}}, \tag{B7}$$

where

$$A_{\rm f} = \int_{x_{\rm f}}^{\infty} dx Z(x). \tag{B8}$$

The $A_{\rm f}$-integral is easy to do numerically. We show the comparison of the numerical and the freeze-out solution of the Lee–Weinberg equation (B1) in Fig. 10 for $\lambda_{hS} = 1$ and $\delta_{\rm f} = 1$. Overall, the freeze-out approximation (B7) is found to be accurate to 0.3%–0.7% over most of the parameter space in our model, the exception being close to the Higgs resonance where the error can reach 1.7%. The dependence of the freeze-out solution on $\delta_{\rm f}$ is at subpercent level for $\delta_{\rm f} = 0.5$–1.5. Let us point out that, if the quantity $\sqrt{g_*}\langle v_{\rm rel}\sigma\rangle$ is weakly dependent on x, one can approximate $A_{\rm f} \approx x_{\rm f}Z_{\rm f}$. This approximation is typically accurate to a few percent at large masses and away from resonances, but it becomes much less accurate near resonances or places where $\sqrt{g_*}\langle v_{\rm rel}\sigma\rangle$ has abrupt features as a function of x.

APPENDIX C: CMB $f_{\rm eff}$ AT WIMP MASSES ABOVE 1 TEV

As a supplement to the results of Ref. [75], in Table I, we give values of $f_{\rm eff}$ for WMAP7 and Planck at WIMP masses m_χ of 3 and 10 TeV.

TABLE I. $f_{\rm eff}$ values for WIMP masses m_χ above 1 TeV, in different primary annihilation channels, for computing WMAP7 (left) and projected Planck (right) constraints. As an example, "μ" denotes $\chi\chi \to \mu\bar{\mu}$, whereas "$V \to \mu$" denotes $\chi\chi \to VV$, followed by $V \to \mu\bar{\mu}$. See Ref. [75] for further details.

$m_\chi \to$	3 TeV	10 TeV	3 TeV	10 TeV
Channel	WMAP7 $f_{\rm eff}$		Planck $f_{\rm eff}$	
e	0.55	0.55	0.59	0.58
μ	0.21	0.21	0.22	0.22
τ	0.18	0.18	0.19	0.19
$V \to e$	0.56	0.56	0.60	0.60
$V \to \mu$	0.20	0.20	0.21	0.21
$V \to \tau$	0.18	0.18	0.19	0.19
$q(u, d, s)$	0.26	0.26	0.28	0.28
c	0.27	0.26	0.28	0.28
b	0.27	0.26	0.28	0.28
t	0.25	0.25	0.27	0.26
γ	0.54	0.52	0.57	0.56
g	0.27	0.26	0.28	0.28
W	0.24	0.24	0.25	0.26
Z	0.22	0.22	0.23	0.23
h	0.25	0.24	0.27	0.26

APPENDIX D: CTA LIKELIHOOD DETAILS

We use the ring method as outlined in Ref. [77], as optimized for CTA candidate array B. The ring method is an advanced version of the standard on-off analysis, where the telescope is pointed slightly away from the Galactic center and the on region (called the "signal region" in the ring method, although it may contain both signal and background) and off region (called the "background region," although it may also contain both signal and background) are defined as different portions of a ring centered on the center of the field of view. A band covering the Galactic plane is excluded from both the signal and background regions. We calculate the signal and background region line-of-sight integrated J factors for DM annihilation toward the Galactic center assuming the Navarro-Frenk-White profile of Ref. [85,121] (namely, a local density of 0.29 GeV/cm^3 and a scale radius of $r_s = 17$ kpc) and a moderate substructure boost factor of around 3, obtaining $J_{\rm ON} = 6.6 \times 10^{21}$ GeV^2 cm^{-5} and $J_{\rm OFF} = 7.7 \times 10^{21}$ GeV^2 cm^{-5}. Even with this mild boost, our signal(on)-region J factor is still approximately a factor of 6 smaller than that given in Ref. [77], most likely because the density profile used in Ref. [77] was based on the Aquarius N-body simulation [122] rather than stellar kinematic fits.

In the absence of any publicly available effective area corresponding to array B, we use the energy-dependent effective area $A_{\rm eff}(E)$ given for an extended array in Ref. [86]. This effective area corresponds to a European baseline array of 25 medium-sized Davis–Cotton telescopes plus an additional (less likely) proposed U.S. contribution of 36 medium-sized Davis–Cotton telescopes. The expected number of events in the observable energy window (approximately 30 GeV–8 TeV for this array) is then

$$\theta_k = \theta_{k,\rm BG} + \theta_{k,\rm DM} = \theta_{k,\rm BG} + t_{\rm obs} J_k \frac{\langle \sigma v_{\rm rel} \rangle}{8\pi m_S^2} \int_0^\infty \sum_i r_i \frac{{\rm d}N_i}{{\rm d}E} A_{\rm eff}(E) {\rm d}E. \quad \text{(D1)}$$

Here, $k \in \{\rm ON, OFF\}$ is a label indicating the region on the sky (signal/on or background/off), whereas $\theta_{k,\rm BG}$ and $\theta_{k,\rm DM}$ are the expected number of events in region k from background processes and DM annihilation, respectively. These events are photons in the case of DM annihilation but will be mostly cosmic rays in the case of the background. The term ${\rm d}N_i/{\rm d}E$ is the differential photon yield from the ith annihilation channel. We assume an integration time $t_{\rm obs}$ of 500 h, as in Ref. [78].

The ring method, and on-off analyses generally, are designed to consider the difference between the observed rates in the signal and background regions. If the background rate is expected to be uniform across the entire ring, then after correction for the ratio of sky areas covered by the signal and background regions $\alpha \equiv \Delta\Omega_{\rm ON}/\Delta\Omega_{\rm OFF}$, the expected difference in the observed counts reflects only signal processes

$$\begin{aligned}\theta_{\rm diff} &\equiv \theta_{\rm ON} - \alpha\theta_{\rm OFF} \\ &= \theta_{\rm ON,BG} + \theta_{\rm ON,DM} - \alpha\theta_{\rm OFF,BG} - \alpha\theta_{\rm OFF,DM} \\ &= \theta_{\rm ON,DM} - \alpha\theta_{\rm OFF,DM}. \end{aligned} \quad \text{(D2)}$$

In the case of the ring geometry that we adopted for array B from Ref. [77], $\Delta\Omega_{\rm ON} = 9.97 \times 10^{-4}$ sr, $\Delta\Omega_{\rm OFF} = 4.05 \times 10^{-3}$ sr $\Rightarrow \alpha = 0.246$. Our value of $\Delta\Omega_{\rm ON}$ is $\sim$4% smaller than stated in Ref. [77], but this can likely be explained by the number of significant figures with which Ref. [77] gave its optimized ring method parameters.

We model the likelihood of observing a given difference $N_{\rm diff} \equiv N_{\rm ON} - \alpha N_{\rm OFF}$ between the on-region and scaled off-region counts, as the difference of two Poisson processes. This is known as a Skellam distribution [123]:

$$\mathcal{L}_S(N_{\rm diff}|\theta_{\rm ON}, \alpha\theta_{\rm OFF}) = e^{-(\theta_{\rm ON}+\alpha\theta_{\rm OFF})} \left(\frac{\theta_{\rm ON}}{\alpha\theta_{\rm OFF}}\right)^{\frac{N_{\rm diff}}{2}} I_{|N_{\rm diff}|}(2\sqrt{\alpha\theta_{\rm ON}\theta_{\rm OFF}}), \quad \text{(D3)}$$

where I_n is the nth modified Bessel function of the first kind. To determine the *expected* limit as we do here, one simply calculates this likelihood assuming $N_{\rm diff} = 0$. Because the dominant background for CTA comes from misidentified electron events, to obtain $\theta_{k,\rm BG}$, we model the expected background flux $\Phi_{\rm BG}$ with an electron spectrum $E^3\Phi_{\rm BG} = 1.5 \times 10^{-2}$ GeV^2 cm^{-2} s^{-1} sr^{-1}, as seen by Fermi [124]. Our final effective likelihood function is the ratio of the signal + background likelihood function [Eq. (D3)]to the background-only version

$$\mathcal{L}_{\mathrm{CTA}}(m_S, \lambda_{hS}) = \frac{\mathcal{L}_{\mathrm{S}}[0|\theta_{\mathrm{ON}}(m_S, \lambda_{hS}), \alpha\theta_{\mathrm{OFF}}(m_S, \lambda_{hS})]}{\mathcal{L}_{\mathrm{S}}(0|\theta_{\mathrm{ON,BG}}, \alpha\theta_{\mathrm{OFF,BG}})}. \tag{D4}$$

In deriving expected limits, we know the best-fit likelihood to occur where the signal contribution is zero, so Eq. (D4) has a maximum $\mathcal{L}_{\mathrm{CTA}} = 1$ at $\langle\sigma v_{\mathrm{rel}}\rangle_0 = 0$. The Skellam distribution is already almost a Gaussian, so by the central limit theorem, the ratio, Eq. (D4), is very close to Gaussian. We can therefore safely consider this likelihood ratio to be χ^2 distributed with 1 degree of freedom and derive confidence limits accordingly.

[1] V. Silveira and A. Zee, Phys. Lett. **161B**, 136 (1985).
[2] J. McDonald, Phys. Rev. D **50**, 3637 (1994).
[3] C. P. Burgess, M. Pospelov, and T. ter Veldhuis, Nucl. Phys. **B619**, 709 (2001).
[4] H. Davoudiasl, R. Kitano, T. Li, and H. Murayama, Phys. Lett. B **609**, 117 (2005).
[5] S. W. Ham, Y. S. Jeong, and S. K. Oh, J. Phys. G **31**, 857 (2005).
[6] B. Patt and F. Wilczek, arXiv:hep-ph/0605188.
[7] D. O'Connell, M. J. Ramsey-Musolf, and M. B. Wise, Phys. Rev. D **75**, 037701 (2007).
[8] X.-G. He, T. Li, X.-Q. Li, and H.-C. Tsai, Mod. Phys. Lett. A **22**, 2121 (2007).
[9] S. Profumo, M. J. Ramsey-Musolf, and G. Shaughnessy, J. High Energy Phys. 08 (2007) 010.
[10] V. Barger, P. Langacker, M. McCaskey, M. J. Ramsey-Musolf, and G. Shaughnessy, Phys. Rev. D **77**, 035005 (2008).
[11] X.-G. He, T. Li, X.-Q. Li, J. Tandean, and H.-C. Tsai, Phys. Rev. D **79**, 023521 (2009).
[12] E. Ponton and L. Randall, J. High Energy Phys. 04 (2009) 080.
[13] R. N. Lerner and J. McDonald, Phys. Rev. D **80**, 123507 (2009).
[14] M. Farina, D. Pappadopulo, and A. Strumia, Phys. Lett. B **688**, 329 (2010).
[15] A. Bandyopadhyay, S. Chakraborty, A. Ghosal, and D. Majumdar, J. High Energy Phys. 11 (2010) 065.
[16] V. Barger, Y. Gao, M. McCaskey, and G. Shaughnessy, Phys. Rev. D **82**, 095011 (2010).
[17] W. -L. Guo and Y.-L. Wu, J. High Energy Phys. 10 (2010) 083.
[18] J. R. Espinosa, T. Konstandin, and F. Riva, Nucl. Phys. **B854**, 592 (2012).
[19] S. Profumo, L. Ubaldi, and C. Wainwright, Phys. Rev. D **82**, 123514 (2010).
[20] A. Djouadi, A. Falkowski, Y. Mambrini, and J. Quevillon, Eur. Phys. J. C **73**, 2455 (2013).
[21] Y. Mambrini, M. H. G. Tytgat, G. Zaharijas, and B. Zaldivar, J. Cosmol. Astropart. Phys. 11 (2012) 038.
[22] A. Drozd, B. Grzadkowski, and J. Wudka, J. High Energy Phys. 04 (2012) 006.
[23] B. Grzadkowski and J. Wudka, Phys. Rev. Lett. **103**, 091802 (2009).
[24] K. Griest and M. Kamionkowski, Phys. Rev. Lett. **64**, 615 (1990).
[25] Y. Mambrini, Phys. Rev. D **84**, 115017 (2011).
[26] I. Low, P. Schwaller, G. Shaughnessy, and C. E. M. Wagner, Phys. Rev. D **85**, 015009 (2012).
[27] A. Djouadi, O. Lebedev, Y. Mambrini, and J. Quevillon, Phys. Lett. B **709**, 65 (2012).
[28] K. Cheung, Y.-L. S. Tsai, P.-Y. Tseng, T.-C. Yuan, and A. Zee, J. Cosmol. Astropart. Phys. 10 (2012) 042.
[29] E. Aprile *et al.* (XENON100 Collaboration), Phys. Rev. Lett. **109**, 181301 (2012).
[30] G. S. Bali *et al.* (QCDSF Collaboration), Phys. Rev. D **85**, 054502 (2012).
[31] G. S. Bali *et al.*, Nucl. Phys. **B866**, 1 (2013).
[32] H. Ohki, K. Takeda, S. Aoki, S. Hashimoto, T. Kaneko, H. Matsufuru, J. Noaki, and T. Onogi (JLQCD Collaboration), Phys. Rev. D **87**, 034509 (2013).
[33] M. Gong *et al.* (xQCD Collaboration), Proc. Sci., LATTICE2011 (2011) 156.
[34] W. Freeman, and D. Toussaint (MILC Collaboration), Phys. Rev. D **88**, 054503 (2013).
[35] M. Engelhardt, Phys. Rev. D **86**, 114510 (2012).
[36] P. Junnarkar and A. Walker-Loud, Phys. Rev. D **87**, 114510 (2013).
[37] R. D. Young, Proc. Sci., LATTICE2012 (2012) 014.
[38] C. Jung (RBC and UKQCD Collaborations), Proc. Sci., LATTICE2012 (2012) 164.
[39] M. Gong *et al.*, Phys. Rev. D **88**, 014503 (2013).
[40] L. Alvarez-Ruso, T. Ledwig, J. M. Camalich, and M. J. Vicente-Vacas, Phys. Rev. D **88**, 054507 (2013).
[41] J. Gasser, H. Leutwyler, and M. E. Sainio, Phys. Lett. B **253**, 252 (1991).
[42] J. Gasser, H. Leutwyler, and M. E. Sainio, Phys. Lett. B **253**, 260 (1991).
[43] B. Borasoy and U.-G. Meissner, Ann. Phys. (N.Y.) **254**, 192 (1997).
[44] J. M. Alarcon, J. M. Camalich, and J. A. Oller, Ann. Phys. (Amsterdam) **336**, 413 (2013).
[45] J. M. Alarcon, L. S. Geng, J. M. Camalich, and J. A. Oller, arXiv:1209.2870.
[46] M. M. Pavan, I. I. Strakovsky, R. L. Workman, and R. A. Arndt, PiN Newslett. **16**, 110 (2002).
[47] H.-Y. Cheng and C.-W. Chiang, J. High Energy Phys. 07 (2012) 009.
[48] G. Belanger, B. Dumont, U. Ellwanger, J. F. Gunion, and S. Kraml, arXiv:1306.2941.
[49] J. M. Cline and K. Kainulainen, J. Cosmol. Astropart. Phys. 01 (2013) 012.
[50] M. E. Peskin, arXiv:1207.2516.
[51] S. Dittmaier *et al.* (LHC Higgs Cross Section Working Group Collaboration), arXiv:1101.0593.
[52] P. Gondolo and G. Gelmini, Nucl. Phys. **B360**, 145 (1991).

[53] B. W. Lee and S. Weinberg, Phys. Rev. Lett. **39**, 165 (1977).
[54] Y. B. Zel'dovich, L. B. Okun', and S. B. Pikel'ner, Sov. Phys. Usp. **8**, 702 (1966).
[55] P. Salati, F. Donato, and N. Fornengo, *Particle Dark Matter: Observations, Models and Searches*, edited by G. Bertone (Cambridge University Press, Cambridge, England, 2010), p. 521.
[56] T. A. Porter, R. P. Johnson, and P. W. Graham, Annu. Rev. Astron. Astrophys. **49**, 155 (2011).
[57] C. E. Yaguna, J. Cosmol. Astropart. Phys. 03 (2009) 003.
[58] A. Goudelis, Y. Mambrini, and C. Yaguna, J. Cosmol. Astropart. Phys. 12 (2009) 008.
[59] C. Arina and M. H. G. Tytgat, J. Cosmol. Astropart. Phys. 01 (2011) 011.
[60] R. Essig, N. Sehgal, and L. E. Strigari, Phys. Rev. D **80**, 023506 (2009).
[61] P. Scott, J. Conrad, J. Edsjo, L. Bergstrom, C. Farnier, and Y. Akrami, J. Cosmol. Astropart. Phys. 01 (2010) 031.
[62] Fermi-LAT Collaboration, Astrophys. J. **712**, 147 (2010).
[63] R. Essig, N. Sehgal, L. E. Strigari, M. Geha, and J. D. Simon, Phys. Rev. D **82**, 123503 (2010).
[64] A. Geringer-Sameth and S. M. Koushiappas, Phys. Rev. Lett. **107**, 241303 (2011).
[65] Fermi-LAT Collaboration, Phys. Rev. Lett. **107**, 241302 (2011).
[66] Y.-L. S. Tsai, Q. Yuan, and X. Huang, J. Cosmol. Astropart. Phys. 03 (2013) 018.
[67] T. Bringmann and C. Weniger, Phys. Dark Univ. **1**, 194 (2012).
[68] N. Padmanabhan and D. P. Finkbeiner, Phys. Rev. D **72**, 023508 (2005).
[69] A. Natarajan and D. J. Schwarz, Phys. Rev. D **80**, 043529 (2009).
[70] S. Galli, F. Iocco, G. Bertone, and A. Melchiorri, Phys. Rev. D **80**, 023505 (2009).
[71] T. R. Slatyer, N. Padmanabhan, and D. P. Finkbeiner, Phys. Rev. D **80**, 043526 (2009).
[72] S. Galli, F. Iocco, G. Bertone, and A. Melchiorri, Phys. Rev. D **84**, 027302 (2011).
[73] D. P. Finkbeiner, S. Galli, T. Lin, and T. R. Slatyer, Phys. Rev. D **85**, 043522 (2012).
[74] T. R. Slatyer, Phys. Rev. D **87**, 123513 (2013).
[75] J. M. Cline and P. Scott, J. Cosmol. Astropart. Phys. 03 (2013) 044; 05 (2013) E01.
[76] C. Weniger, P. D. Serpico, F. Iocco, and G. Bertone, Phys. Rev. D **87**, 123008 (2013).
[77] M. Doro *et al.* (CTA Collaboration), Astropart. Phys. **43**, 189 (2013).
[78] M. Wood, J. Buckley, S. Digel, S. Funk, D. Nieto, and M. A. Sanchez-Conde, arXiv:1305.0302.
[79] M. Cirelli, G. Corcella, A. Hektor, G. Hütsi, M. Kadastik, P. Panci, M. Raidal, F. Sala, and A. Strumia, J. Cosmol. Astropart. Phys. 03 (2011) 051; 10 (2012) E01.
[80] P. Gondolo, J. Edsjo, P. Ullio, L. Bergstrom, M. Schelke, and E. A. Baltz, J. Cosmol. Astropart. Phys. 07 (2004) 008.
[81] E. Komatsu *et al.* (WMAP Collaboration), Astrophys. J. Suppl. Ser. **192**, 18 (2011).
[82] P. A. R. Ade *et al.* (Planck Collaboration), arXiv:1303.5076.
[83] L. Lopez-Honorez, O. Mena, S. Palomares-Ruiz, and A. C. Vincent, J. Cosmol. Astropart. Phys. 07 (2013) 046.
[84] S. Galli, T. R. Slatyer, M. Valdes, and F. Iocco, Phys. Rev. D **88**, 063502 (2013).
[85] J. F. Navarro, C. S. Frenk, and S. D. M. White, Astrophys. J. **490**, 493 (1997).
[86] T. Jogler, M. D. Wood, and J. Dumm (CTA Collaboration), AIP Conf. Proc. **1505**, 765 (2012).
[87] J. R. Ellis, K. A. Olive, and C. Savage, Phys. Rev. D **77**, 065026 (2008).
[88] Y. Akrami, C. Savage, P. Scott, J. Conrad, and J. Edsjo, J. Cosmol. Astropart. Phys. 04 (2011) 012.
[89] G. Bertone, D. G. Cerdeno, M. Fornasa, R. Ruiz de Austri, C. Strege, and R. Trotta, J. Cosmol. Astropart. Phys. 01 (2012) 015.
[90] M. A. Shifman, A. I. Vainshtein, and V. I. Zakharov, Phys. Lett. **78B**, 443 (1978).
[91] S. Fiorucci (LUX Collaboration), arXiv:1301.6942.
[92] M. Woods (LUX Collaboration), arXiv:1306.0065.
[93] E. Aprile (XENON1T Collaboration), arXiv:1206.6288.
[94] P. Beltrame (XENON Collaboration), arXiv:1305.2719.
[95] S. Andreas, T. Hambye, and M. H. G. Tytgat, J. Cosmol. Astropart. Phys. 10 (2008) 034.
[96] S. Andreas, C. Arina, T. Hambye, F.-S. Ling, and M. H. G. Tytgat, Phys. Rev. D **82**, 043522 (2010).
[97] T. Bringmann, X. Huang, A. Ibarra, S. Vogl, and C. Weniger, J. Cosmol. Astropart. Phys. 07 (2012) 054.
[98] C. Weniger, J. Cosmol. Astropart. Phys. 08 (2012) 007.
[99] E. Tempel, A. Hektor, and M. Raidal, J. Cosmol. Astropart. Phys. 09 (2012) 032.11 (2012) A01.
[100] M. Su and D. P. Finkbeiner, arXiv:1206.1616.
[101] A. Hektor, M. Raidal, and E. Tempel, arXiv:1209.4548.
[102] D. P. Finkbeiner, M. Su, and C. Weniger, J. Cosmol. Astropart. Phys. 01 (2013) 029.
[103] D. Whiteson, J. Cosmol. Astropart. Phys. 11 (2012) 008.
[104] Fermi-LAT Collaboration, arXiv:1305.5597.
[105] J. M. Cline, Phys. Rev. D **86**, 015016 (2012).
[106] D. Hooper and L. Goodenough, Phys. Lett. B **697**, 412 (2011).
[107] D. Hooper and T. Linden, Phys. Rev. D **84**, 123005 (2011).
[108] K. N. Abazajian and M. Kaplinghat, Phys. Rev. D **86**, 083511 (2012).
[109] D. Hooper and T. R. Slatyer, Phys. Rev. D **88**, 043513 (2013).
[110] S. Weinberg, Phys. Rev. Lett. **110**, 241301 (2013).
[111] K. Enqvist, D. G. Figueroa, and R. N. Lerner, J. Cosmol. Astropart. Phys. 01 (2013) 040.
[112] G. Degrassi, S. Di Vita, J. Elias-Miro, J. R. Espinosa, G. F. Giudice, G. Isidori, and A. Strumia, J. High Energy Phys. 08 (2012) 098.
[113] M. Gonderinger, Y. Li, H. Patel, and M. J. Ramsey-Musolf, J. High Energy Phys. 01 (2010) 053.
[114] M. Kadastik, K. Kannike, A. Racioppi, and M. Raidal, J. High Energy Phys. 05 (2012) 061.
[115] V. Barger, P. Langacker, M. McCaskey, M. Ramsey-Musolf, and G. Shaughnessy, Phys. Rev. D **79**, 015018 (2009).
[116] A. Sirlin and R. Zucchini, Nucl. Phys. **B266**, 389 (1986).
[117] L. Bergstrom, G. Bertone, J. Conrad, C. Farnier, and C. Weniger, J. Cosmol. Astropart. Phys. 11 (2012) 025.

[118] M. Drees and K.-i. Hikasa, Phys. Lett. B **240**, 455 (1990); **262**, 497(E) (1991).
[119] E. W. Kolb and M. S. Turner, *The Early Universe*, Frontiers in Physics Vol. 69 (Addison-Wesley, Redwood City, California, 1990).
[120] G. Steigman, B. Dasgupta, and J. F. Beacom, Phys. Rev. D **86**, 023506 (2012).
[121] G. Battaglia, A. Helmi, H. Morrison, P. Harding, E. W. Olszewski, M. Mateo, K. C. Freeman, J. Norris, and S. A. Shectman, Mon. Not. R. Astron. Soc. **364**, 433 (2005); **370**, 1055(E) (2006).
[122] V. Springel, J. Wang, M. Vogelsberger, A. Ludlow, A. Jenkins, A. Helmi, J. F. Navarro, C. S. Frenk, and S. D. M. White, Mon. Not. R. Astron. Soc. **391**, 1685 (2008).
[123] J. G. Skellam, J. R. Stat. Soc. **109**, 296 (1946).
[124] A. A. Abdo *et al.* (Fermi LAT Collaboration), Phys. Rev. Lett. **102**, 181101 (2009).